



## Adhesion measurement of highly-ordered TiO<sub>2</sub> nanotubes on Ti-6Al-4V alloy

Masoud Sarraf<sup>1,2</sup>, Bushroa Abdul Razak<sup>1,2,3,4,\*</sup>, Ryan Crum<sup>5</sup>, Carlos Gámez<sup>4</sup>, Brian Ramirez<sup>4</sup>, Noor Hayaty Binti Abu Kasim<sup>6</sup>, Bahman Nasiri-Tabrizi<sup>7,\*\*</sup>, Vijay Gupta<sup>3,8</sup>, Nazatul Liana Sukiman<sup>2</sup>, Wan Jeffrey Basirun<sup>9</sup>

<sup>1</sup>Center of Advanced Manufacturing and Material Processing, Department of Engineering, University of Malaya, Kuala Lumpur 50603, Malaysia

<sup>2</sup>Department of Mechanical Engineering, Faculty of Engineering, University of Malaya

<sup>3</sup>Department of Mechanical Engineering, Faculty of Engineering, University of UCLA, Los Angeles, CA 90032, United States

<sup>4</sup>Department of Mechanical and Aerospace Engineering, University of California, Los Angeles, CA 90095-1597, United States

<sup>5</sup>Physics Division, Lawrence Livermore National Laboratory, Livermore, CA 94550, United States

<sup>6</sup>Department of Restorative Dentistry, Faculty of Dentistry, University of Malaya, Kuala Lumpur, Malaysia

<sup>7</sup>Advanced Materials Research Center, Materials Engineering Department, Najafabad Branch, Islamic Azad University, Najafabad, Isfahan, Iran

<sup>8</sup>Department of Bioengineering, University of California, Los Angeles, CA 90095-1597, United States

<sup>9</sup>Department of Chemistry, Faculty of Science, University of Malaya, 50603 Kuala Lumpur, Malaysia

Received 5 July 2017; Received in revised form 30 October 2017; Accepted 4 December 2017

### Abstract

Self-assembled nanotubular arrays on Ti alloys could be used for more effective implantable devices in various medical approaches. In the present work, the adhesion of TiO<sub>2</sub> nanotubes (TiO<sub>2</sub> NTs) on Ti-6Al-4V (Ti64) was investigated by laser spallation and scratch test techniques. At first, electrochemical anodization was performed in an ammonium fluoride solution dissolved in a 90:10 ethane-1,2-diol (ethylene glycol) and water solvent mixture. This process was performed at room temperature (23 °C) at a steady potential of 60 V for 1 h. Next, the TiO<sub>2</sub> nanotubes layer was heat-treated to improve the adhesion of the coating. The formation of self-organized TiO<sub>2</sub> nanotubes as well as the microstructural evolution, are strongly dependent on the processing parameters and subsequent annealing. From microscopic analysis, highly oriented arrays of TiO<sub>2</sub> nanotubes were grown by thermal treatment for 90 min at 500 °C. Further heat treatment above 500 °C led to the detachment of the nanotubes and the complete destruction of the nanotubes occurred at temperature above 700 °C. Scratch test analysis over a constant scratch length (1000 μm) indicated that the failure point was shifted from 247.4 to 557.9 μm while the adhesion strength was increased from ~862 to ~1814 mN after annealing at 500 °C. The adhesion measurement determined by laser spallation technique provided an intrinsic adhesion strength of 51.4 MPa for the TiO<sub>2</sub> nanotubes on the Ti64 substrate.

**Keywords:** titania, nanotubes, adhesion, laser spallation, Ti-6Al-4V

\*Corresponding author: tel: +60 379675239

e-mail: [bushroa@um.edu.my](mailto:bushroa@um.edu.my) (A.R. Bushroa)

\*\*Corresponding author: tel: +98 9132275822

e-mail: [bahman\\_nasiri@hotmail.com](mailto:bahman_nasiri@hotmail.com) (B. Nasiri-Tabrizi)

### I. Introduction

Over the past decade, there is a growing number of patients with damaged tissues which require replacements with synthetic components such as dental im-

plants, hip replacements, etc. Among the various synthetic components, metallic implants such as cobalt-based alloys, stainless steels and titanium-based alloys are the most common in orthopaedic applications. Titanium-based alloys, such as Ti64, have been receiving significant attention for medical applications due to their lightness, inertness, high corrosion resistance, bio-compatibility, strength and non-allergic complications. However, the failure of hip/femur titanium alloy joints due to the friction has been widely observed. Thus, to reduce the possible dangers during healing time of the bioactive ceramics, surface improvement is effective for further modification of the biocompatibility of titanium alloy joints. In fact, one of the most effective approaches to improve the fixity between calcified tissues and metallic implants, and augmenting the implant lifetime is to coat the surface of titanium-based implants with a bioactive ceramics such as hydroxyapatite/titanium oxide composite (HA/TiO<sub>2</sub>) which could boost quick bonding to the native bone. The other benefit of coating orthopaedic implants with bioactive ceramics is the mitigation of ion release from the metallic substrate, or increase in the corrosion resistance [1–3].

The weak tribological performances of Ti-based alloys are associated with the crystal structure, electron and crystal configuration, as well as lubrication features. This problem can be solved by altering the nature of the surface [4]. According to the literature, the formation of a TiO<sub>2</sub> passive film provides the required biocompatibility and inertness needed in titanium alloy implants [5]. So far, considerable research effort has been focused on various nanostructured coatings for improved osseointegrative properties and mechanical features (microhardness and fretting fatigue life) of the metallic implants [6–8]. Recently, nanostructured TiO<sub>2</sub> films have been studied due to the various advantages over conventional micro-sized counterparts, such as high mechanical and tribological properties, good corrosion resistance and enhanced biocompatibility [9–13]. Nanotubular TiO<sub>2</sub> could be prepared by electrochemical anodization (one- or two step approaches), which is the most widely practised technique [14].

The stability of the thin films is represented by the hardness, Young's modulus and the adhesion between the coating layer and the undercoat [15,16]. Thus, an improvement in the adhesion between the thin films and implant materials is obviously desirable, where the integrity of the undercoat/thin layer interface strongly depends on the efficiency and dependability of the coating device [17]. Numerous methods have been employed to examine the adhesion feature of the coatings, where the most common are the peel examination [18], bulge analysis [19], laser spallation [20], thin layer tensile assessment [21] and scratch analysis [22]. Among these techniques, the scratch adhesion test provides a quantitative assessment of the cohesion of the coatings to the undercoat, notwithstanding a fundamental lack of realization of the mechanics of the method. On the other

hand, the laser spallation technique (LST) is a qualitative method and involves basic aspects with regards to the computable adhesion strength [15]. In this approach, a laser pulse of sufficient energy and time duration is transformed into a compressive stress wave, which is spread throughout the undercoat headed for the free surface of the coating. The compressive signal is reflected from the sample's free surface to release the tension, to maintain a traction-free surface. When the magnitude of the reflected wave is sufficient, the reflected tensile wave delaminates the thin film coating from its interface. A multistep process is utilized to determine the crucial stress state which is required to delaminate the entire coating. A displacement interferometry is initially utilized to obtain the free surface displacement (unconstrained film surface) and to determine the compressive stress state which propagates to the film's free-surface. Then, the interferometrically measured stress state is used as an input to an ABAQUS finite element simulation that matches the experimental setup in order to specify the tensile stress state at the film/substrate interface. Therefore, one can take advantage of LST and scratch test to provide a holistic adhesion measurement before the implantation process. However, to the best of our knowledge, there are still no reports on the adhesion measurement of highly-ordered TiO<sub>2</sub> nanotubes on Ti64 by laser spallation technique.

Hereon, the surface modification of biomedical Ti64 was performed by electrochemical anodization using a DC power source. To crystallize the nanotubes and enhance the adhesion of the coating, heat treatment was performed after the anodization process. The structural features and morphological evolution of the experimental outputs were examined to gain a better understanding of the process parameters' influence on the adhesion strength of the nanotubular coating to the Ti64. In addition, LST was utilized to appraise the adhesion strength of the nanostructured coatings. The results of this study could initiate a new field of investigation on the adhesion properties of highly-ordered nanotubular arrays.

## II. Materials and experimental procedures

### 2.1. Undercoat features

Ti64 plates (15 × 15 × 2 mm<sup>3</sup>, E Steel Sdn. Bhd. Malaysia) were utilized as the undercoats. The substrates were ground with SiC papers and thereupon were polished in wet diamond slurry to a shining finish, followed by sonication at 40 °C for 10 min. Finally, the undercoats were rinsed with distilled water (three times) and dehydrated for 60 min at 100 °C.

### 2.2. Growth of TiO<sub>2</sub> nanotubes

A one-pot anodization process with different electrolyte solutions was used to prepare the TiO<sub>2</sub> nanotubes with similar procedures as already reported [9]. Hereon, the undercoats were anodized in a NH<sub>4</sub>F (Sigma-Aldrich Co.) solution dissolved in a 90:10 ethane-1,2-

diol (EG, J.T. Baker Co.) and water solvent mixture at room temperature. A DC power source was utilized in the anodizing process, where the undercoat was the anode while a graphite rod (diameter of 5 mm) was the cathode. In all experiments, the gap between the positive and negative terminals was held steady at 20 mm. The anodizing process was carried out at a steady potential of 60 V for 1 h. Finally, the anodized specimens were annealed in an argon-filled furnace for 90 min at 500 and 700 °C at a heating/cooling rate of 5 °C/min.

### 2.3. Characterization

#### Phase and microstructural analysis

X-ray diffraction (XRD) measurements were performed by PANalytical Empyrean system (Netherlands) with Cu-K $\alpha$  radiation, with  $2\theta$  range of 20–80°. Software PANalytical X'Pert HighScore was utilized to analyse the X-ray profiles, and the reflections were matched with JCPDS standards. The morphological evolution of the coating was also assessed by means of a high-resolution field emission scanning electron microscope (FESEM, FEI Quanta 200 F).

#### Adhesion strength

The adhesion strength between the coatings (TiO<sub>2</sub>NTs) and undercoat (Ti64) was determined quantitatively by a microscratch tester (Micro Materials Ltd., Wrexham, UK). Here, a pre-scratch scan was performed using an ultra-low contact force to assess the baseline sample topography. Afterwards, the scratch examination was replicated three times within the specified load range using a diamond indenter (with radius of 25.0 ± 2.0 μm and angle of 90.0 ± 5.0°). The experiment was performed over a 1000 μm track at a scan speed of 5 mm/s. The subsequent damage profile was investigated by an optical microscope (Olympus BX61, Tokyo, Japan). In addition, friction measurements were also acquired throughout the scan process.

#### Adhesion measurements by laser spallation

The laser spallation facility, developed by Gupta and co-workers [23,24] has been extensively utilized to determine the adhesion strength between metal, ceramics and polymer coatings on pre-engineered surfaces [25,26]. In this study, a modified version of the laser spallation system was utilized to calculate the interfacial tensile strength of highly-ordered TiO<sub>2</sub> nanotubes on Ti64 substrates, as shown in Fig. 1.

A nominal 8 ns Nd:YAG laser pulse was impinged over a 3.0 mm diameter area on a 0.5-μm-thick laser absorbing Al layer, which was packed between a transparent 20–50 μm thick layer of water-glass and the back surface of the Ti64 undercoat. Upon absorbing the laser energy, the constrained Al film exfoliates and generates a compressive stress wave (with a 1–2 ns rise-time and 16–20 ns duration) towards the front surface of the substrate, where the test coating (TiO<sub>2</sub> nanotubes) is located. The compressive stress wave was reflected from

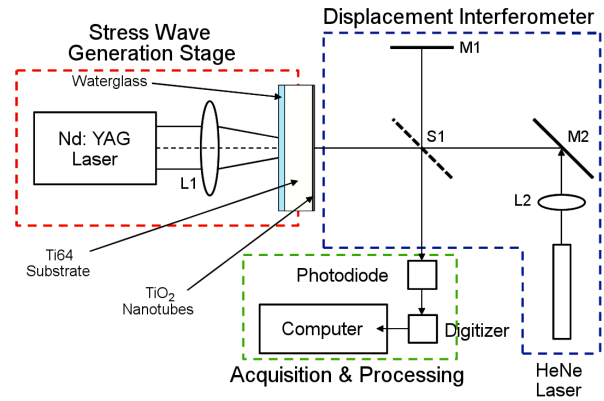


**Figure 1. Modified laser spallation set-up for determining the interfacial strength of highly-ordered TiO<sub>2</sub> nanotubes coated on Ti64 substrates**

the coating's free surface into a tensile wave, which promotes the spallation (or absolute elimination) of the coating, if the magnitude of the tensile signal is greater than the adhesion strength of the interface. Thus, the laser energy increased until the magnitude of the reflected tensile stress signal is sufficient to delaminate the entire substrate/coating interface.

The interfacial adhesion strength was measured using a high-tech optical interferometer, to determine the transient free surface displacements that are related to the stress wave profile. Here, it was not possible to measure the incident time-dependent stress wave profile  $\sigma(t)$  generated on the Ti64 substrate during the spallation of the TiO<sub>2</sub> nanotubes. Instead, the  $\sigma(t)$  was obtained in a separate experiment where an isolated Ti64 sample was shock-loaded under the same stress wave generated conditions (laser fluence and thickness of Ti64 substrate, and water-glass layers), where the interface failure was observed. The free surface velocity  $v(t)$  of the Ti64 substrate was obtained from the transient free surface displacements using the optical interferometer and was used to calculate the  $\sigma(t)$  from the following equation:

$$\sigma(t) = \frac{\rho \cdot c_0}{2} \left[ v \left( t + \frac{h}{c} \right) - v \left( t - \frac{h}{c} \right) \right] \quad (1)$$

where  $c_0 = 2289$  m/s,  $\rho$  and  $h$  are the longitudinal wave speed in the substrate medium (Ti64), the substrate density, and substrate thickness, respectively [27].

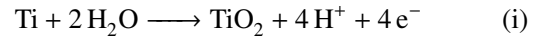
In these experiments, the test coating thickness was significantly thinner than the length of the stress wave. Therefore, the destructive interference of the compressive stress wave with the reflected tensile wave at the interface must be accounted for. Thus, the exact stress-state at the substrate/coating interface was determined using a finite element (FE) simulation with the interferometrically measured stress state,  $\sigma(t)$ , as an input. The FE model was implemented in ABAQUS as a 2D planar finite element simulation. The Ti64 substrate and TiO<sub>2</sub> nanotubes were defined as deformable solids with the corresponding material properties: density, Poisson's ra-

tio and elastic modulus. All materials were defined to the exact scale observed in the experiments. The Ti64 substrate was modeled to be 2 mm thick while the TiO<sub>2</sub> nanotubes were 3 μm tall with 120 nm inner diameter and 20 nm nanotube wall thickness. The substrate and coating were tie-constrained to ensure displacement continuity on the interface. In addition, the mesh comprised of explicit plane stress elements and the size was kept uniform in all domains to prevent the spurious wave reflectance effects which occur at the material interface. Furthermore, a time step of 0.2 ns was used to satisfy the numerical constant linking Δt to the element size Δx through the wave velocity c, Δt < Δx/c. The local stresses obtained from the FEM model correspond to the stresses for elements at the Ti64/TiO<sub>2</sub> nanotube interface. Thus, the peak tensile stress at the location of failure from the FEM model was taken as the interfacial tensile strength between the Ti64 undercoat and the TiO<sub>2</sub>NTs. Furthermore, since the experiments were performed at extremely high deformation rates, the inelastic components during the separation process were suppressed and the interfacial strength is a function of the microstructure and chemistry of the interface, making it an intrinsic interfacial strength.

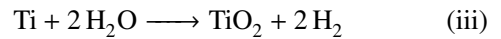
### III. Growth mechanism of TiO<sub>2</sub> nanotubes

Generally, self-organized TiO<sub>2</sub>NTs can be grown by a simple electrochemical anodization of metallic titanium or its alloys undercoat under controlled conditions. The electrochemical oxidation process could be controlled by various parameters such as anodization voltage, anodization time and electrolyte composition. However, the growth of TiO<sub>2</sub>NTs principally depends on the concentration of the F<sup>-</sup> electrolyte [11]. The growth of nanotubular arrays in such electrolytes occurs because of two challenging processes: i) the hydrolysis of metallic titanium (TiO<sub>2</sub> growth) and ii) chemical dissolution

of oxide layer at the oxide/electrolyte interface. When the process is initiated, a preliminary oxide film is generated from the interaction of the surface Ti<sup>4+</sup> ions and the O<sup>2-</sup> in the solution, which homogeneously spreads across the surface. At the anode, Ti<sup>4+</sup> ions are liberated due to the oxidation of the metal, while the dominant reaction at the cathode is the hydrogen gas evolution [11]:



Accordingly, the general equation for oxide generation is as follows:



On the other hand, the F<sup>-</sup> ions could penetrate the oxide and hydrated film; i.e. the F<sup>-</sup> ion migrating through the anodic film under applied electric field could react with the Ti<sup>4+</sup>. The dominant reactions are as follows:



As shown in Fig. 2a, a thin layer of oxide formation occurs on the Ti64 surface, upon the anodization process. From Fig. 2b, the formation of small pits is due to the localized dissolution of the oxide film, causing the barrier film underneath the pits to be moderately thin. This effect increases the intensity of the electric field through the residual barrier film, initiating additional pore growth as shown in Fig. 2c. It has been proven that the electric field assisted dissolution has no signif-

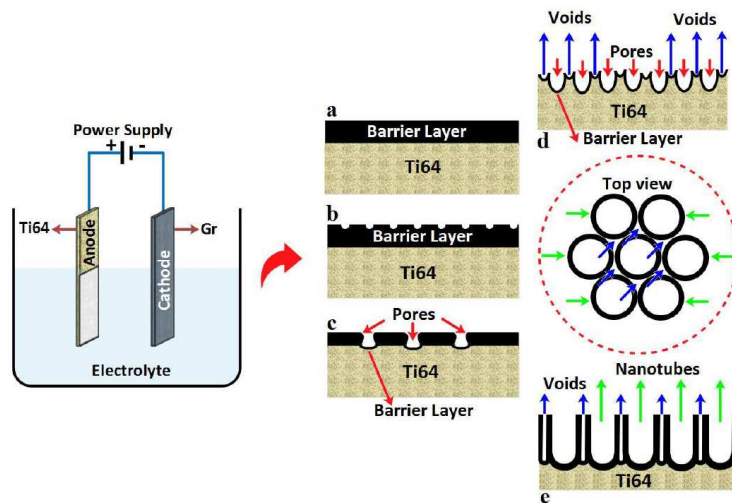
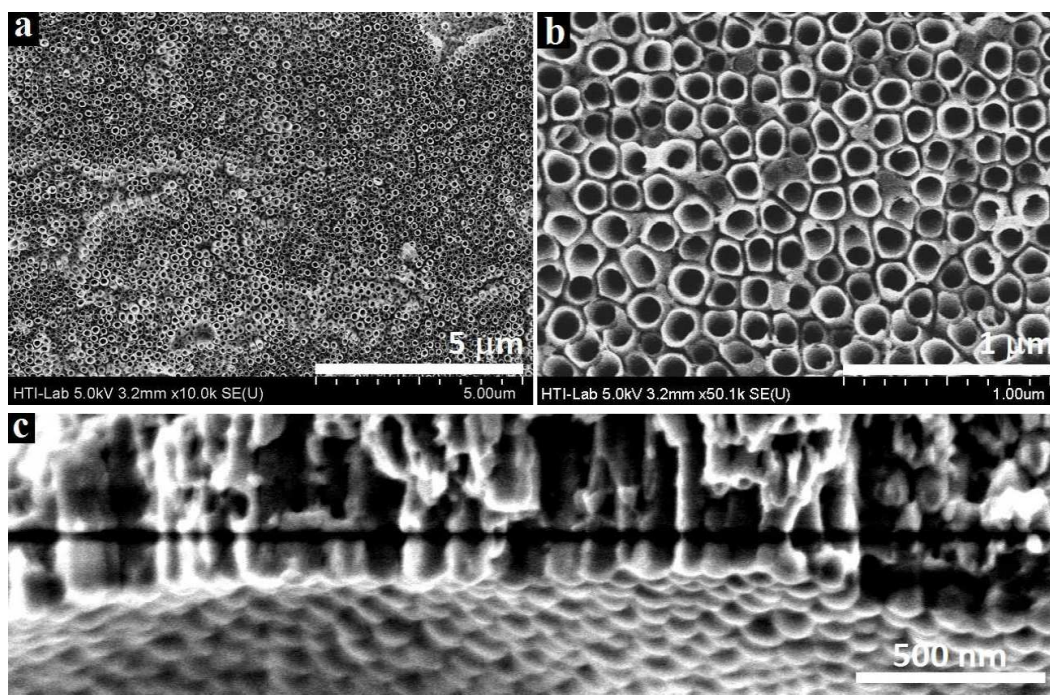


Figure 2. Schematic of the anodization cell and generation of TiO<sub>2</sub>NTs at steady voltage: a) oxide film generation, b) pit development, c) growth of the pit, d) oxidation and field assisted dissolution of the substrate area between the pores and e) completely expanded nanotubular configuration



**Figure 3.** FESEM images of Ti64 surface after one pot anodization with exposure time of 1 h in 0.35%  $\text{NH}_4\text{F}$  electrolyte solution (90 EG: 10 water) at a steady potential of 60 V - top view (a,b) and bottom (c)

icant effect on the pore entrance. Therefore, the pore entrance stays moderately narrow whereas the electric field is scattered in the bowed surface underneath the pores which results in pore broadening, in addition to the deepening of the pores [28]. Since the bond energy of Ti–O is large, it may be inferred that  $\text{TiO}_2$  pores with narrow walls could be formed owing to the moderately lower ion dynamism and comparatively higher chemical solubility of the oxide in solution. Hence, some unoxidized surface could be present between the pores. When the pores deepen, the electric field at the unoxidized surface is amplified, thus accelerating the field assisted growth and dissolution of the oxide layer. These steps occur simultaneously, where well-defined inter-pore voids form concurrently with the pores (Fig. 2d). Thenceforth, both pores and tubes enlarge in equilibrium. The length of nanotubular arrays increases until the rate of the anodization equals the rate of chemical dissolution on the surface of the nanotubular arrays. After reaching equilibrium, the length of nanotubes will be independent of the anodization time, as determined for a given electrolyte concentration and anodization potential.

## IV. Results and discussions

### 4.1. Microstructural features

Since the structure and dimensions of the nanotubular arrays play a critical role in the biomedical functionality, microstructural characterization is a fundamental step to understand the biomedical behaviour [29]. Figure 3 shows the FESEM images of Ti64 surface after one-pot anodization with an immersion time of 1 h in

0.35%  $\text{NH}_4\text{F}$  electrolyte solution (90 EG: 10 water) at a steady potential of 60 V.

As mentioned earlier, during the initial stages of anodization, asymmetrical pits were formed as a result of the localized dissolution of the oxide film followed by the pits transformation to larger pores. With a prolonged anodization time, uniformly distributed pores are formed, where the pore formation is a consequence of the local surface perturbations [30]. When the anodization time is extended to 1 h, significant changes from nonporous to nanotubular structure were observed as shown in Fig. 3a. As can be seen, highly ordered  $\text{TiO}_2\text{NTs}$  were formed after 1 h of anodization, where the nanotubular arrays are homogeneously dispersed on the surface. From the higher magnification micrograph in Fig. 3b, the mean inner diameter is 120 nm. During the early stages of anodization, the field-assisted dissolution predominates during the chemical dissolution process due to the high electric field across the electrode. When the anodization continues as the oxide layer thickens, the chemical dissolution dominates over the field-assisted dissolution. This effect increases the dimension and compression of the pores. Following this stage, the pore formation occurs by interior changes at the oxide/substrate interface, which leads to the generation of hollow tubular oxide configuration.

As shown in Fig. 3c, the  $\text{TiO}_2\text{NTs}$  underneath layer demonstrates a series of evenly spaced “bumps” which signify the pore tips of each individual nanotube [11,17,31]. Given that the barrier film underneath the  $\text{TiO}_2\text{NTs}$  is scalloped, this film can be separated to the upper part as the pure barrier film and lower section as the interfacial barrier layer [11]. The upper part is

considered to be purely oxide, whereas the lower section is considered as a combination of oxide and undercoat material (Ti64). When the oxide film underneath the pore is exposed to chemical dissolution, it becomes thinner over time. The electric field-assisted dissolution becomes more dominant as the thickness decreases in this area, thereby the pores penetrate through the undercoat, making the nanotubular arrays progressively longer. Nevertheless, as the voltage is incessantly applied, anodization could re-occur underneath the pores, with the formation of nanotubular arrays with closed bottom [32]. To assess the effect of subsequent annealing on the morphological transition, heat treatment was carried out with constant heating/cooling rate at 500 and 700 °C for 90 min in an argon gas furnace. Figure 4 shows the top view FESEM micrographs of the 1 h processed sample after annealing at 500 °C at different magnifications.

The results for the TiO<sub>2</sub> nanotubes annealed at higher temperature (700 °C) are also provided in Fig. 5. From Fig. 4a,b, a highly ordered TiO<sub>2</sub> nanotube array was formed during annealing at 500 °C for 90 min. Obviously, there were no considerable alterations in the morphological characteristics after annealing at this temperature. Accordingly, there were no significant changes in the morphology and tube diameter during annealing at 500 °C as shown in Fig. 4c,d. It has been found that the nanotubes could collapse at particular annealing conditions such as high temperature and extended annealing time [33]. Here, the surface morphology of the nanotubular arrays were transformed after annealing for 90 min at 700 °C as illustrated in Fig. 5. Hereon,

the nanotubes were completely destroyed after 90 min of annealing at 700 °C (Fig. 5a,b), whereby the tubular configuration was changed to a coarse particulate structure (Fig. 5c). Similar results of the collapse of the TiO<sub>2</sub> nanotubes due to the annealing at higher temperatures were previously reported [34]. This indicates that higher temperature exceeding 500 °C is the main reason for the collapse of the TiO<sub>2</sub> nanotubular arrays.

#### 4.2. XRD analysis

Figure 6 displays the XRD profiles of the substrate (Ti64), the 1 h anodized sample and the sample annealed for 90 min at 500 °C. From Fig. 6a, the XRD reflection of the undercoat illustrates merely the diffraction peaks of titanium (JCPDS#005-0682) at  $2\theta = 35.1^\circ$ ,  $38.4^\circ$ ,  $40.2^\circ$ ,  $53.1^\circ$ ,  $63.1^\circ$ ,  $70.6^\circ$  and  $76.4^\circ$ , which is attributed to the (100), (002), (101), (102), (110), (112) and (201) planes, respectively. After 1 h anodization, a coating with an amorphous structure was formed as shown in Fig. 6b. Nevertheless, the as-prepared coating is not fully amorphous. There are some characteristic peaks corresponding to the anatase TiO<sub>2</sub> (JCPDS#01-071-1166).

During annealing at 500 °C, a highly crystalline single anatase phase with tetragonal symmetry (JCPDS#01-071-1166) was formed as a consequence of the thermally induced crystallization. Accordingly, new diffraction peaks ((101) plane at  $2\theta = 25.3^\circ$ , (004) plane at  $2\theta = 38.4^\circ$ , (200) plane at  $2\theta = 48.1^\circ$ , (105) plane at  $2\theta = 53.2^\circ$ , and (201) plane at  $2\theta = 55.2^\circ$ ) corresponding to TiO<sub>2</sub> (anatase) became apparent in the XRD profile. Based on the XRD results, the

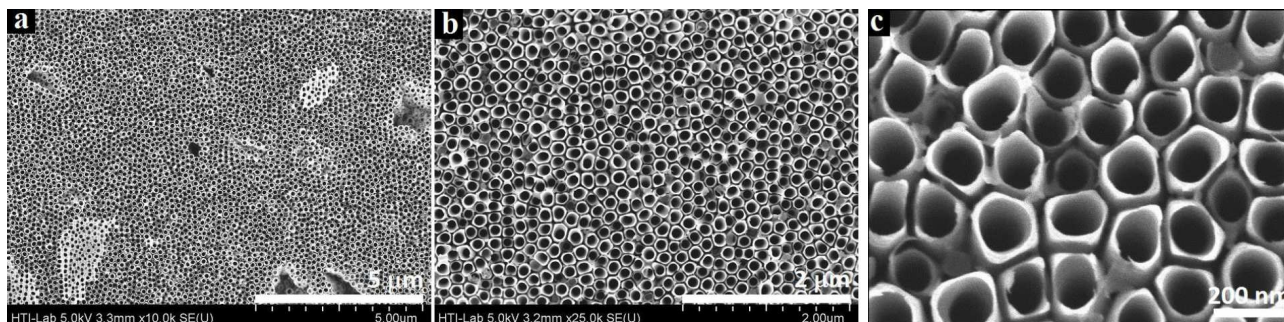


Figure 4. Top view FESEM micrographs of the 1 h processed sample after annealing at 500 °C for 90 min at different magnifications

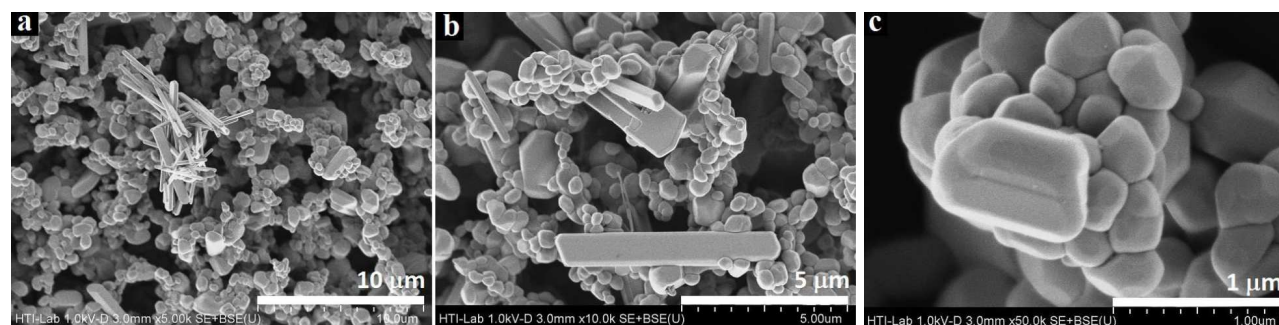


Figure 5. FESEM micrographs of the 1 h processed specimen after annealing at 700 °C for 90 min at different magnifications; (a,b) detachment of nanotubes and (c) formation of a coarse particle structure

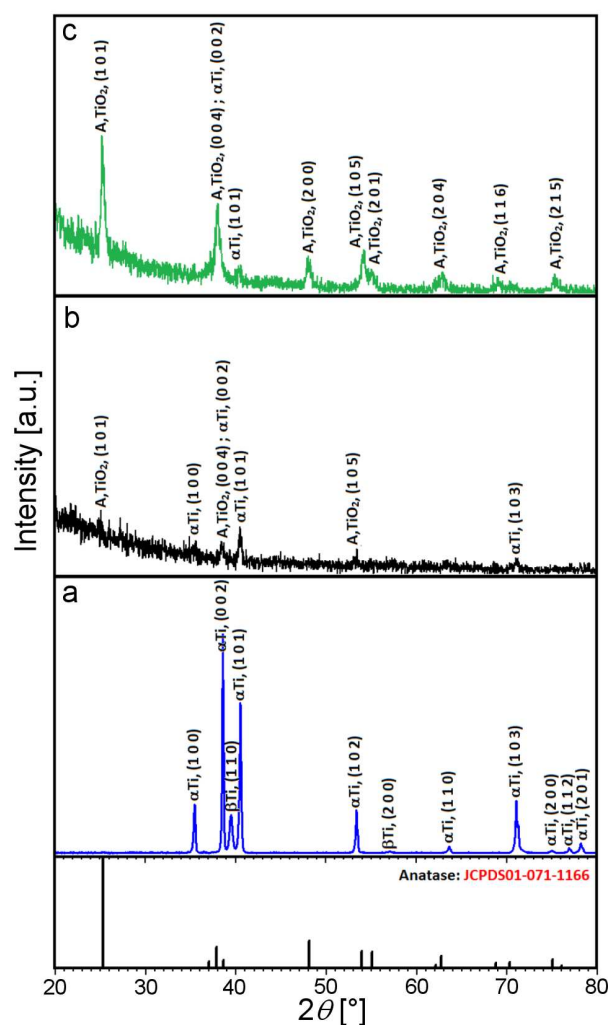


Figure 6. XRD patterns of the substrate (a), 1 h processed specimen before (b) and after (c) annealing at 500 °C/90 min

phase composition and preferred crystal orientation may change after the subsequent annealing process. In addition, the fraction of anatase is likely altered at higher temperatures due to the anatase-to-rutile phase transition.

#### 4.3. Adhesion strength measured by scratch method

As mentioned earlier, the stability of a thin layer coating does not only depend on the elastic modulus and hardness of the coating, but also on the adherence between the coating and the undercoat [15,16]. Here, both quantitative and qualitative assessments of the adherence of TiO<sub>2</sub> nanotubes to the Ti64 substrate are provided using scratch test and LST method, respectively.

Figure 7 shows the optical image of a scratch profile and diagrams of depth, load, friction and coefficient of friction (COF) versus distance for the 1 h anodized specimen at a steady potential of 60 V. Hereon, the orientation of scratch was from left to right. With regards to the crucial load determination, there are different methods such as microscopic assessment, acoustic emission examination, tridimensional force recording, acoustic reflection mode scanning microscope (ARRM) and evalu-

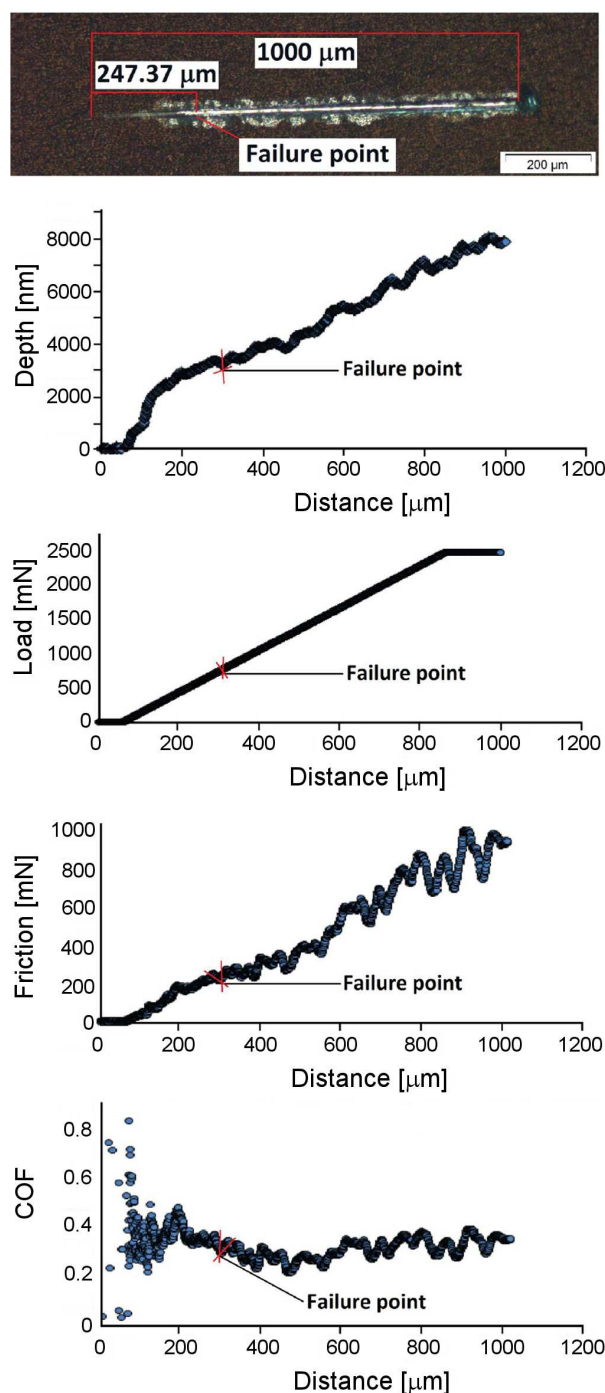


Figure 7. Optical image of scratch profile (a) and diagrams of depth (b), load (c), friction (d) and COF (e) versus scan distance related to the 1 h anodized specimen

ation of the diffusion depth of the scratch point [35]. In this study, optical microscopy was used to examine the surface destruction caused by the scratch test. The gap between the start or end point and the scratched region is related to the load and can be quantified by an optical microscope. Generally, the critical loads, i.e.  $L_{e-p}$ ,  $L_{c1}$ ,  $L_{c2}$ , and  $L_{c3}$ , are defined by the sudden alterations in the graph of depth against distance. The  $L_{e-p}$  alludes to an elastic-to-plastic evolution and cohesive defeat, whereas  $L_{c1}$  is related to lower critical load and displays the on-

set of equal and rim cracking. In addition,  $L_{c2}$  and  $L_{c3}$  are attributed to superior crucial load which is specified by fractional delamination of the coating and to a full coating defeat, respectively [36,37].

In the present case, the respective defeat modes were identified to denote the critical loads needed to rupture the bond between the TiO<sub>2</sub>NTs and the undercoat. It is obvious that the nanotubular configuration was initially in an elastic-to-plastic evolution mode.  $L_{c1}$ , showed up as cracking on the trackside followed by a gentle tensile cracking in the direction of the scratch. By increasing the scratch load, the delamination trackside appeared which is symbolized as  $L_{c2}$ . A further increase in the load led to a variety of failures along the scratch path involving trackside cracking, delamination and chipping  $L_{c3}$ . From Figs. 7a to c, the length of scratch and defeat points of the coated sample are 1000 and 247.4 μm, respectively, where the adhesion strength was ~862 mN. Additionally, the calculated friction and COF were 186.883 mN and 0.40, respectively (Figs. 7d,e).

Figure 8a shows the optical image of the scratch profile and diagrams of depth, load, friction and COF versus distance, for the 1 h processed specimen after thermal treatment for 90 min at 500 °C. Over the same scratch length (1000 μm), the failure point was shifted to 557.9 μm and adhesion strength was increased to ~1814 mN after annealing at 500 °C.

For further investigation, the scratch hardness test was evaluated to determine the resistance of TiO<sub>2</sub> nanotubular arrays to perennial defect under the action of the stylus tip. Since the diamond stylus moves tangentially along the surface, the scratch hardness test contains different combination of surface properties. This examination presents the measurements of the remaining scratch width which the stylus removes, to determine the scratch hardness number. Hence, this analysis indicates the perennial defect due to the scratching and not the temporary state of merged elastic and plastic defeat of the surface. Given that the stress state at the indenter tip is a function of practical force and contact geometry, the amplitude of the scratch hardness number depends on both the applied load and the radius of the indenter tip. This assumes that the hemispherically-tipped stylus creates a groove whose leading surface has a radius of curvature  $r$ , or the tip radius of the stylus. Here, the critical load was specified at the beginning of the coating defeat associated with an onset of visibility of the undercoat inside the scratch path. In this approach, the friction coefficient can also be determined at the critical load [31,38,39]. The scratch hardness  $HS_p$  was estimated using the following equation:

$$HS_p = \frac{8P}{\pi \cdot w^2} \quad (2)$$

where  $HS_p$ ,  $P$  and  $w$  are the scratch hardness number, typical force and width of scratch, respectively.

Based on the obtained data, the scratch hardness of the anodized sample before and after annealing was 0.45

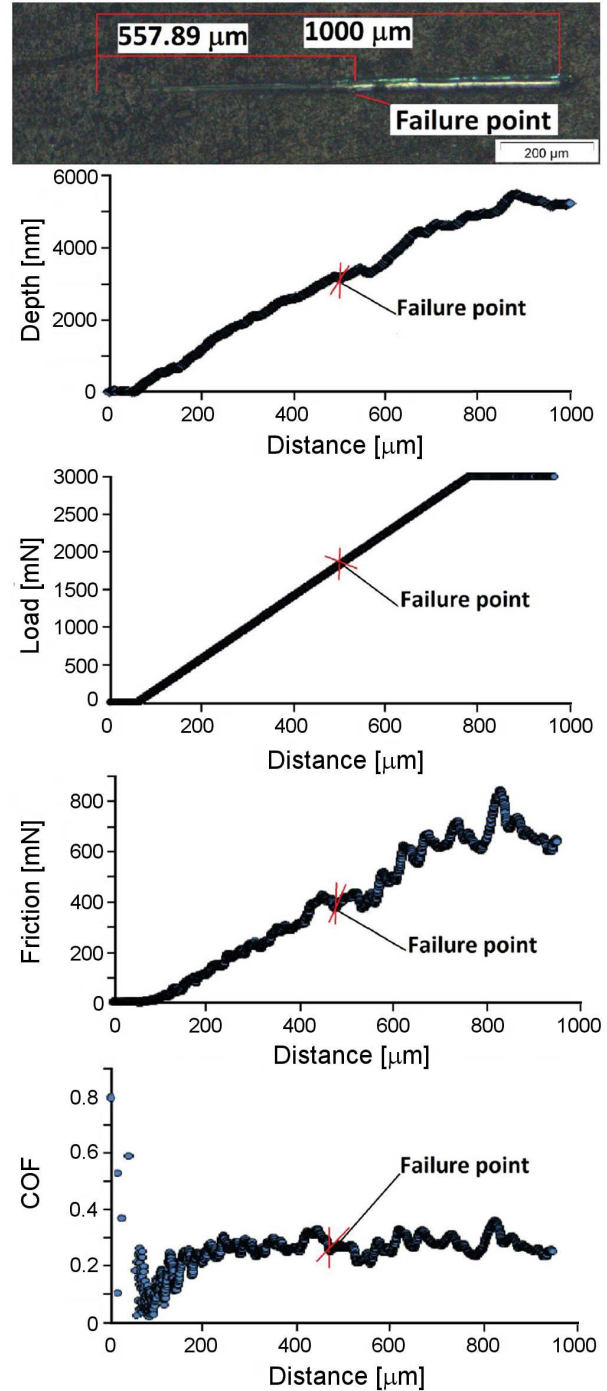


Figure 8. Optical image of scratch profile (a) and diagrams of depth (b), load (c), friction (d), and COF (e) versus distance for the 1 h anodized sample after thermal treatment at 500 °C

and 5.86 GPa, respectively. These results show that the scratch hardness increased by over an order of magnitude after the annealing process compared to the untreated sample.

#### 4.4. Adhesion measurement by LST method

Since the amplitude of the stress wave is proportional to the laser fluence, the increase in the fluence results in an increase in the stress wave magnitude. Therefore,

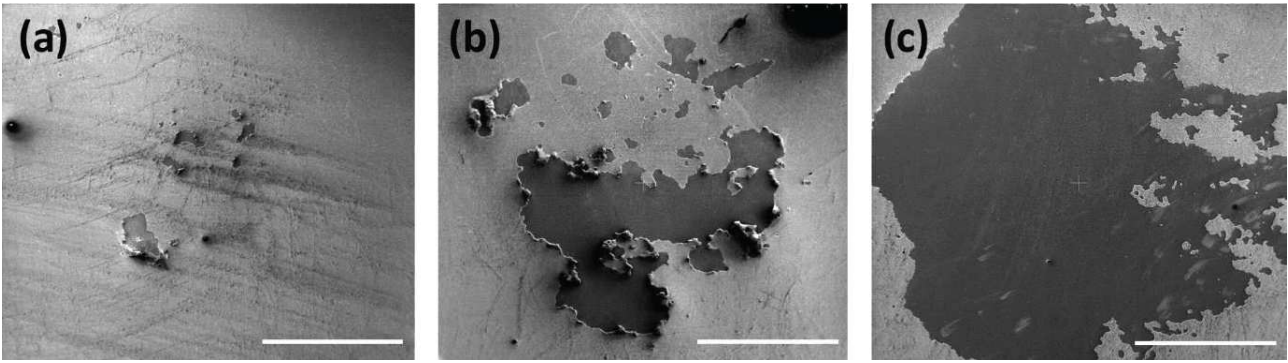


Figure 9. Scanning electron micrographs of TiO<sub>2</sub> film tested by LST at laser fluence of: a) 29.1, b) 34.5, and c) 70.7 kJ/m<sup>2</sup> (all scale bars are 1 mm)

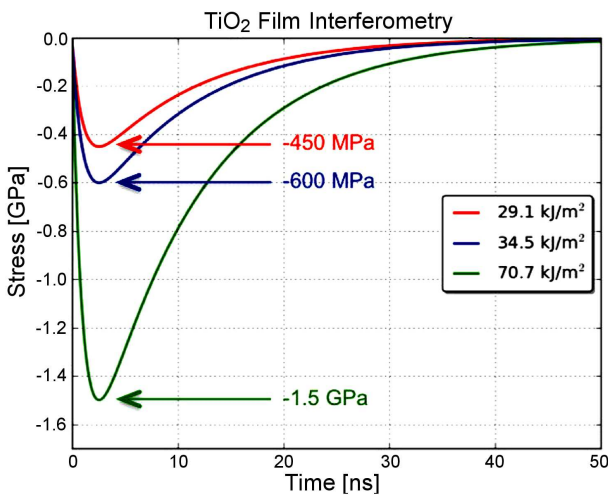


Figure 10. Interferometric measurements of the stress wave profile

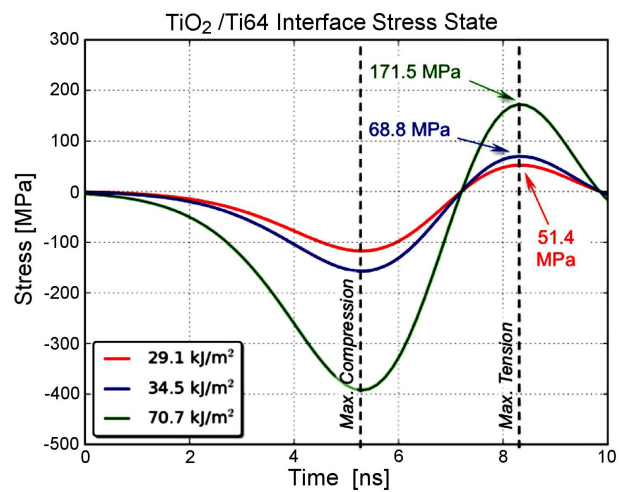


Figure 11. Interface stress-time profile obtained from the FEM simulations

the laser spallation experiments were conducted under increasing laser fluence values (14.1 to 70.7 kJ/m<sup>2</sup>) to determine the critical value that corresponds to the onset of delamination as well as the full spallation of the TiO<sub>2</sub>/Ti64 interface. Figure 9 shows the SEM micrographs of progressive interface failure under increasing laser fluence. The initial delamination of the TiO<sub>2</sub> nanotubes from the Ti64 substrate occurred at 29.1 kJ/m<sup>2</sup> (Fig. 9a), partial spallation at 34.5 kJ/m<sup>2</sup> (Fig. 9b), while the full spallation of the TiO<sub>2</sub> nanotubes occurred at 70.7 kJ/m<sup>2</sup> (Fig. 9c).

The quantitative measurements of the substrate free surface displacements and velocity were obtained using Michelson interferometer as presented earlier (Fig. 1). These results were used to obtain the input compressive wave profile (using Eq. (1)) for the FEM analysis. The interferometrically measured compressive stress state profile in the substrate for the laser fluence levels that resulted in spallation (29.1, 34.5, and 70.7 kJ/m<sup>2</sup>) are shown in Fig. 10. The substrate's compressive stress states were 450 MPa, 600 MPa, and 1.5 GPa at laser fluence values of 29.1, 34.5, and 70.7 kJ/m<sup>2</sup>, respectively.

The exact stresses at the TiO<sub>2</sub>/Ti64 interface were then obtained using the FEM model from the compressive stress state profile inputs (Fig. 10) obtained from

interferometry. Figure 11 shows the interface stress-time profile obtained from the FEM simulation under the laser fluence of 29.1, 34.5, and 70.7 kJ/m<sup>2</sup>. From these plots, it can be seen that the interface was initially loaded under compression, due to the incoming laser generated stress wave followed by tension loading, as the reflected tensile wave reaches the interface. The interfacial tensile strength of the TiO<sub>2</sub>/Ti64 interface was 51.4 MPa. This value corresponds to the initial delamination and failure of the interface at a laser fluence of 29.1 kJ/m<sup>2</sup>. Since 29.1 kJ/m<sup>2</sup> is the fluence of the initial failures, this value was taken as the inherent strength of the interface. The partial spallation of the TiO<sub>2</sub> nanotubes was 68.8 MPa (34.5 kJ/m<sup>2</sup>) while the complete spallation of the coating was 171.5 MPa (70.7 kJ/m<sup>2</sup>). All values correspond to the peak tensile stresses at the interface under corresponding laser fluence.

## V. Conclusions

The electrochemical anodization of Ti-6Al-4V alloy was performed at room temperature at a constant potential of 60 V for 1 h for the growth of self-ordered nanotubular arrays on the surface. When the anodization time was extended to 1 h, significant changes from

nanoporous to nanotubular structure were observed. From the FESEM observations, a highly ordered TiO<sub>2</sub> nanotube array was formed during heat treatment for 90 min at 500 °C. A further increase in the temperature to 700 °C completely destroyed the nanotubes, where the TiO<sub>2</sub>NTs were converted to a coarse grain structure. According to the XRD data, a coating with an amorphous structure was formed after 1 h anodization. During annealing at 500 °C, a highly crystalline single anatase phase was formed due to the thermally induced crystallization and consequently new diffraction peaks attributed to the anatase phase were obvious in the XRD reflection.

According to the scratch test, the adhesion strength of the anodized sample before and after annealing was ~862 mN and ~1814 mN, respectively. These results show that the adhesion strength increases after annealing as compared to the untreated sample. The results of adhesion measurement by laser spallation technique showed that the intrinsic strength of the TiO<sub>2</sub> film adherence to the Ti64 substrate was 51.4 MPa for the initial stages of spallation, 68.8 MPa for significant spallation and 171.5 MPa for complete spallation of the TiO<sub>2</sub> film.

**Acknowledgements:** The authors would like to acknowledge the University of Malaya, Malaysia and University of California, Los Angeles for providing necessary resources and facilities for this study. This research was fully funded by the University of Malaya with the high impact research grant numbers of RP032C-15AET and PG081-2014B. The authors are also grateful to Research Affairs of Islamic Azad University, Najafabad Branch for supporting of this research.

## References

1. D. Nunamaker, *Total Joint Replacement - Textbook of Small Animal Orthopaedics*, Lippincott, Philadelphia, PA, 1985.
2. R.R. Kumar, M. Wang, "Functionally graded bioactive coatings of hydroxyapatite/titanium oxide composite system", *Mater. Lett.*, **55** [3] (2002) 133–137.
3. K. Kawagoe, M. Saito, T. Shibuya, T. Nakashima, K. Hino, H. Yoshikawa, "Augmentation of cancellous screw fixation with hydroxyapatite composite resin (CAP) in vivo", *J. Biomed. Mater. Res.*, **53** [6] (2000) 678–684.
4. H. Guleryuz, H. Cimenoglu, "Surface modification of a Ti-6Al-4V alloy by thermal oxidation", *Surf. Coat. Tech.*, **192** [2-3] (2005) 164–170.
5. T. Monetta, A. Acquesta, A. Carangelo, F. Bellucci, "TiO<sub>2</sub> nanotubes on Ti dental implant. Part 2: EIS characterization in Hank's solution", *Metals*, **7** (2017) 220.
6. L. Salou, A. Hoornaert, G. Louarn, P. Layrolle, "Enhanced osseointegration of titanium implants with nanostructured surfaces: An experimental study in rabbits", *Acta Biomater.*, **11** [1] (2015) 494–502.
7. X. Zhang, Y. Ma, N. Lin, X. Huang, R. Hang, A. Fan, B. Tang, "Microstructure, antibacterial properties and wear resistance of plasma Cu-Ni surface modified titanium", *Surf. Coat. Tech.*, **232** [15] (2013) 515–520.
8. H. Wu, X. Zhang, X. He, M. Li, X. Huang, R. Hang, B. Tang, "Wear and corrosion resistance of anti-bacterial Ti-Cu-N coatings on titanium implants", *Appl. Surf. Sci.*, **317** [30] (2014) 614–621.
9. M. Sarraf, E. Zalnezhad, A.R. Bushroa, A. Hamouda, A. Rafieerad, B. Nasiri-Tabrizi, "Effect of microstructural evolution on wettability and tribological behavior of TiO<sub>2</sub> nanotubular arrays coated on Ti-6Al-4V", *Ceram. Int.*, **41** [6] (2015) 7952–7962.
10. W.-Q. Yu, J. Qiu, L. Xu, F.-Q. Zhang, "Corrosion behaviors of TiO<sub>2</sub> nanotube layers on titanium in Hank's solution", *Biomed. Mater.*, **4** [6] (2009) 065012.
11. C.A. Grimes, G.K. Mor, *TiO<sub>2</sub> Nanotube Arrays: Synthesis, Properties, and Applications*, Springer Science & Business Media, 2009.
12. Y. Xu, M. Wang, J.M. Bell, C. Yan, "Toughness and toughening mechanisms of porous thin films", pp. 179–224 in *Thin Films and Coatings: Toughening and Toughness Characterization*, Ed. Zhang, Sam, CRC Press (Taylor & Francis Group), Boca Raton, FL, 2015.
13. X. Zhang, M. Li, X. He, X. Huang, R. Hang, B. Tang, "Effects of silver concentrations on microstructure and properties of nanostructured titania films", *Mater. Desig.*, **65** (2015) 600–605.
14. E. Zalnezhad, E. Maleki, S.M. Banihashemian, J.W. Park, Y.B. Kim, M. Sarraf, A.A.D.M. Sarhan, S. Ramesh, "Wettability, structural and optical properties investigation of TiO<sub>2</sub> nanotubular arrays", *Mater. Res. Bull.*, **78** (2016) 179–185.
15. S.K. Venkataraman, J.C. Nelson, A.J. Hsieh, D.L. Kohlstedt, W.W. Gerberich, "Continuous microscratch measurements of thin film adhesion strengths", *J. Adhes. Sci. Tech.*, **7** [12] (1993) 1279–1292.
16. W.Y. Zhang, G.Z. Li, Y.N. Li, Z.T. Yu, Z.P. Xi, "Fabrication of TiO<sub>2</sub> nanotube arrays on biologic titanium alloy and properties", *Trans. Nonferrous Met. Soc. China*, **17** (2007) s692–s695.
17. S. Baradaran, W.J. Basirun, E. Zalnezhad, M. Hamdi, A.A. Sarhan, Y. Alias, "Fabrication and deformation behaviour of multilayer Al<sub>2</sub>O<sub>3</sub>/Ti/TiO<sub>2</sub> nanotube arrays", *J. Mech. Behav. Biomed. Mater.*, **20** [1] (2013) 272–282.
18. C. Kovalchick, A. Molinari, G. Ravichandran, "An experimental investigation of the stability of peeling for adhesive tapes", *Mech. Mater.*, **66** [1] (2013) 69–78.
19. G. Machado, G. Chagnon, D. Favier, "Induced anisotropy by the Mullins effect in filled silicone rubber", *Mechan. Mater.*, **50** [1] (2012) 70–80.
20. V. Gupta, A.S. Argon, D.M. Parks, J.A. Cornie, "Measurement of interface strength by a laser spallation technique", *J. Mech. Phys. Solids*, **40** [1] (1992) 141–180.
21. R.W. Hoffman, "Nanomechanics of thin films: Emphasis: Tensile properties", *MRS Proceedings*, **130** (1988) 295.
22. A.J. Perry, "Scratch adhesion testing of hard coatings", *Thin Solid Films*, **107** [2] (1983) 167–180.
23. V. Gupta, J. Yuan, "Measurement of interface strength by the modified laser spallation technique. II. Applications to metal/ceramic interfaces", *J. Appl. Phys.*, **74** [4] (1993) 2397.
24. J. Yuan, V. Gupta, A. Pronin, "Measurement of interface strength by the modified laser spallation technique. III. Experimental optimization of the stress pulse", *J. Appl. Phys.*, **74** [4] (1993) 2405.
25. V. Gupta, "System and method for measuring the interface tensile strength of planar interfaces", US Patent 5 438 402, August, 1995.

26. J. Shim, V. Hagerman, B. Wu, V. Gupta, "Measurement of the tensile strength of cell-biomaterial interface using the laser spallation technique", *Acta Biomater.*, **4** [6] (2008) 1657–1668.
27. G. Youssef, R. Crum, S.V. Prikhodko, D. Seif, G. Po, N. Ghoniem, S. Kodambaka, V. Gupta, "The influence of laser-induced nanosecond rise-time stress waves on the microstructure and surface chemical activity of single crystal Cu nanopillars", *J. Appl. Phys.*, **113** [8] (2013) 084309.
28. G.K. Mor, O.K. Varghese, M. Paulose, K. Shankar, C.A. Grimes, "A review on highly ordered, vertically oriented TiO<sub>2</sub> nanotube arrays: Fabrication, material properties, and solar energy applications", *Sol. Energ. Mater. Sol. Cells*, **90** [14] (2006) 2011–2075.
29. M. Sarraf, B.A. Razak, A. Dabbagh, B. Nasiri-Tabrizi, N.H.A. Kasim, W.J. Basirun, "Optimizing PVD conditions for electrochemical anodization growth of well-adherent Ta<sub>2</sub>O<sub>5</sub> nanotubes on Ti-6Al-4V alloy", *RSC Adv.*, **6** [82] (2016) 78999–79015.
30. G. Crawford, N. Chawla, K. Das, S. Bose, A. Bandyopadhyay, "Microstructure and deformation behavior of biocompatible TiO<sub>2</sub> nanotubes on titanium substrate", *Acta Biomater.*, **3** [3] (2007) 359–367.
31. M. Sarraf, E. Zalnezhad, A.R. Bushroa, A. Hamouda, S. Baradaran, B. Nasiri-Tabrizi, A. Rafieerad, "Structural and mechanical characterization of Al/Al<sub>2</sub>O<sub>3</sub> nanotube thin film on TiV alloy", *Appl. Surf. Sci.*, **321** [1] (2014) 511–519.
32. Z. Lockman, S. Sreekantan, S. Ismail, L. Schmidt-Mende, J.L. Macmanus-Driscoll, "Influence of anodisation voltage on the dimension of titania nanotubes", *J. Alloy. Compd.*, **503** [2] (2010) 359–364.
33. A.E.R. Mohamed, S. Rohani, "Modified TiO<sub>2</sub> nanotube arrays (TNTAs): progressive strategies towards visible light responsive photoanode, a review", *Energ. Environ. Sci.*, **4** [4] (2011) 1065–1086.
34. L. Mohan, C. Anandan, V. Rajendran, "Electrochemical behaviour and bioactivity of self-organized TiO<sub>2</sub> nanotube arrays on Ti-6Al-4V in Hanks' solution for biomedical applications", *Electrochim. Acta*, **155** [1] (2015) 411–420.
35. J. Sekler, P.A. Steinmann, H.E. Hintermann, "The scratch test: Different critical load determination techniques", *Surf. Coat. Tech.*, **36** [1-2] (1988) 519–529.
36. A.R. Bushroa, H.H. Masjuki, M.R. Muhamad, B.D. Beake, "Optimized scratch adhesion for TiSiN coatings deposited by a combination of DC and RF sputtering", *Surf. Coat. Tech.*, **206** [7] (2011) 1837–1844.
37. Q.M. Mehran, A.R. Bushroa, M.A. Fazal, "Evaluation of CrAlN multilayered coatings deposited by PVD magnetron sputtering", *J. Adhes. Sci. Tech.*, **29** [19] (2015) 2076–2089.
38. ASTM 2003 – Standard test method for scratch hardness of materials using a diamond stylus.
39. R. Jaworski, L. Pawlowski, F. Roudet, S. Kozerski, F. Petit, "Characterization of mechanical properties of suspension plasma sprayed TiO<sub>2</sub> coatings using scratch test", *Surf. Coat. Tech.*, **202** [12] (2008) 2644–2653.